Estimating Hurricane Wind Structure in the Absence of Aircraft Reconnaissance

JAMES P. KOSSIN,* JOHN A. KNAFF,+ HOWARD I. BERGER,* DERRICK C. HERNDON,*
THOMAS A. CRAM,+ CHRISTOPHER S. VELDEN,* RICHARD J. MURNANE,# AND JEFFREY D. HAWKINS@

*Cooperative Institute for Meteorological Satellite Studies, University of Wisconsin—Madison, Madison, Wisconsin
+Cooperative Institute for Research in the Atmosphere, Colorado State University, Fort Collins, Colorado
#Risk Prediction Initiative, Bermuda Biological Station for Research, Garrett Park, Maryland
@Naval Research Laboratory, Monterey, California

(Manuscript received 30 December 2005, in final form 12 June 2006)

ABSTRACT

New objective methods are introduced that use readily available data to estimate various aspects of the two-dimensional surface wind field structure in hurricanes. The methods correlate a variety of wind field metrics to combinations of storm intensity, storm position, storm age, and information derived from geostationary satellite infrared (IR) imagery. The first method estimates the radius of maximum wind (RMW) in special cases when a clear symmetric eye is identified in the IR imagery. The second method estimates RMW, and the additional critical wind radii of 34-, 50-, and 64-kt winds for the general case with no IR scene–type constraint. The third method estimates the entire two-dimensional surface wind field inside a storm-centered disk with a radius of 182 km. For each method, it is shown that the inclusion of infrared satellite data measurably reduces error. All of the methods can be transitioned to an operational setting or can be used as a postanalysis tool.

1. Introduction

At present, there are a number of methods available for measuring or estimating surface wind fields around tropical cyclones, each with its own strengths and shortcomings. Satellite-based microwave scatterometers generally perform best in low-wind and low-precipitation environments (Zeng and Brown 1998; Weissman et al. 2002; Yueh et al. 2003) and are thus useful for estimating surface winds in the tropical cyclone (TC) outer core away from the high-wind and high-precipitation region of the eyewall. Satellite-based passive microwave instruments such as the Special Sensor Microwave Imager (SSM/I) are routinely applied to the estimation of surface wind over open water but are also limited to the outer core when estimating TC winds (Goodberlet et al. 1989). Similarly, geostationary satellite cloud-track winds (e.g., Velden et al. 2005) can be deduced in the outer core away from the obscuring effects of the cirrus shield that typically resides over the inner core. The underlying surface winds can then be estimated by reducing the cloud-track winds to the surface (Dunion et al. 2002; Dunion and Velden 2002).

Further information on outer-core surface winds is obtained by global positioning system (GPS) dropwindsondes (Hock and Franklin 1999) released from Gulfstream-IV jet aircraft that routinely fly in the western Atlantic basin (Aberson and Franklin 1999; Aberson 2002) and more recently from Astra SPX jet aircraft flying in the northwest Pacific basin (Wu et al. 2005). For reasons of safety, these small high-altitude jet aircraft avoid the turbulent area of the TC inner core.

While there are a variety of sources for TC outer-core wind data, the only inner-core wind data that are routinely available at present are collected by low-altitude aircraft reconnaissance. These aircraft—the National Oceanic and Atmospheric Administration (NOAA) WP-3D and United States Air Force WC-130—typically fly radial flight legs toward and away from the TC center. Most of the radial legs are flown at an altitude of ~3 km and the wind at that level is measured by inertial and GPS navigation systems on board the aircraft. The flight-level wind data can be reduced

---

Corresponding author address: Dr. James P. Kossin, Cooperative Institute for Meteorological Satellite Studies, University of Wisconsin—Madison, Madison, WI 53706.
E-mail: kossin@ssec.wisc.edu

DOI: 10.1175/WAF985.1

to the surface using empirically derived relationships (e.g., Franklin et al. 2003).

In addition to flight-level measurements, dropwindsondes are regularly deployed from the WP-3D and WC-130 aircraft, and surface wind below the WP-3D aircraft is estimated along the flight path by a passive microwave sensor—the Stepped-Frequency Microwave Radiometer (Uhlhorn and Black 2003). In addition to the onboard wind sensors, the WP-3D aircraft are equipped with Doppler radar that can be operated in dual-Doppler mode to measure the three-dimensional wind structures in the precipitating inner core (Reasor et al. 2000; Marks 2003), but these data are not available operationally and require significant postprocessing.

At present, sampling of the inner cores of hurricanes by low-altitude aircraft is performed routinely only in the Atlantic basin. Aircraft reconnaissance in the eastern and central Pacific is occasionally tasked at the discretion of the National Hurricane Center. In all other TC-prone ocean basins, in situ information about inner-core winds is based entirely on occasional serendipitous sources such as ships, buoys, and island-based meteorological measurements. Furthermore, because of the range limitations of the aircraft, westward-tracking hurricanes in the Atlantic are not investigated until they are close enough to aircraft bases required for takeoff and landing. Thus, storms that are far out to sea, but still pose a threat to shipping and marine interests, are not sampled by aircraft and information about inner-core wind is often unavailable for many days.

Here, we introduce new methods for estimating TC surface wind structure in the absence of aircraft reconnaissance, with an emphasis on the TC inner core. The methods use information regarding current storm intensity, position, and age—which are always operationally available—and information related to the cloud structures measured by geostationary infrared (IR) imagery, which is available globally every 30 min.

The data used in this study comprise flight-level wind profile data from U.S. Air Force WC-130 and NOAA WP-3D reconnaissance archives (Jorgensen 1984; Kossin and Eastin 2001), IR imagery from the Cooperative Institute for Research in the Atmosphere (CIRA) Tropical Cyclone IR Archive (Zehr 2000), best-track position fixes (Jarvinen et al. 1984), operational "working best track" intensity and position fixes, and "extended best track" information, which includes measurements of critical wind radii (Kimball and Mulekar 2004). The data cover the North Atlantic hurricane seasons from 1995 to 2004. All IR imagery was renavigated to storm-centric coordinates using cubic-spline-interpolated best-track positions (Kossin 2002).

We will introduce three methods for estimating the TC surface wind field structure. The first method (section 2a) takes direct advantage of the relationship between TC eye size and the radius of maximum wind (RMW). The second method (section 2b) applies extended best-track information to directly estimate the critical wind radii of 34-, 50-, 64-kt winds (R34, R50, and R64, respectively), and RMW. In the third method (section 2c) we apply flight-level wind profiles, working best-track information regarding storm intensity and position, and IR data to train a simple regression that can then be used to estimate the entire two-dimensional inner-core surface wind field. In sections 2a–c, we will perform independent tests of the method and document error, and section 3 will summarize the results.

2. Estimation of surface wind field structure

a. *Direct estimation of RMW in clear-eye cases*

The relationship between the transverse (divergent) and primary (rotational) circulations in TCs is well established (Shapiro and Willoughby 1982). Typically, the primary updraft core in the eyewall is within a few kilometers of the RMW and the updraft core is generally flanked by radially broader regions of weaker subsidence (e.g., Jorgensen et al. 1985). As a storm matures, the area of subsidence inside the RMW typically forms an eye while the subsiding area outside the RMW forms the relatively convection free area referred to sometimes as the moat (Kossin et al. 2000, Rozoff et al. 2006). When a clear symmetric eye becomes apparent in the IR imagery, we can then directly exploit this relationship with our data by considering the relationship between IR-measured eye size and RMW.

To form an algorithm that can be used to estimate RMW, we formed a sample of the IR-measured eye size in cases of well-defined clear and symmetric eyes, and regressed aircraft-measured RMW onto this. We also have an a priori expectation that the RMW is correlated to storm intensity (hereafter referred to as $V_{\max}$) and storm latitude (Shea and Gray 1973; Mueller et al. 2006), but we found that including these as additional predictors in the regression did not have much effect on the error or variance explained. In this case, there is a such a strong one-to-one relationship between IR-measured eye size and RMW that the inclusion of additional predictors that have a less direct relationship to RMW made virtually no additional contribution.

The sample of aircraft-measured RMW was constructed by individual scrutiny of flight-level tangential wind profiles from the NOAA WP-3D database. Reduction of the flight-level RMW to the surface was performed assuming a 45° outward slope with height from 1 km above the surface to flight level, and no slope below 1 km (Willoughby 1998; Jorgensen 1984; Corbosiero et al. 2005). Cases where the RMW was associated with a secondary wind maximum within a secondary eyewall (Willoughby et al. 1982; Samsury and Zipser 1995) were not included in the sample, and the algorithm will suffer from transient errors related to eyewall replacement cycles. Under the limitation that the ubiquitous cirrus canopy of hurricanes is opaque in IR wavelengths, there is no present method for identifying secondary eyewalls with IR imagery and our algorithm is necessarily constrained by this.

The IR-measured eye size was calculated as follows:

1) Identify the preceding storm-centered IR image nearest in time to the aircraft reconnaissance fix.
2) Measure the mean cloud-top brightness temperature above the eyewall (denoted $BT_{eyewall}$). The mean is calculated in an annulus $40 \leq r \leq 70$ km. We found that this annulus was a good compromise for capturing more eyewall cloud-top BT with minimal contribution from the warmer BT found in the eye and outside the eyewall in the moat.
3) If $BT_{eyewall} \leq -50°C$, which is true in most cases, we measure the distance from storm center to the −45°C isotherm along the four cardinal directions: N, E, S, and W. We found that the radius of the −45°C isotherm serves as a good proxy for the circular region of steep BT gradient separating the warm eye and cold eyewall cloud tops, but without introducing the noise inherent in calculating gradients directly from the BT data. The requirement that $BT_{eyewall} \leq -50°C$ better guarantees that the −45°C isotherm will lie within the eye–eyewall interface.
4) Occasionally, it is found that $BT_{eyewall} > -50°C$. In these somewhat rare cases, the IR-measured eye size is better represented by measuring the distance from storm center to a warmer isotherm as follows:
    (a) measure the warmest pixel in a storm-centered disk $r \leq 30$ km (denoted BT_{eye});
    (b) the warmer isotherm is then given by $(BT_{eye} + 2BT_{eyewall})/3$; we found that shifting the isotherm in this way does a good job of placing it within the eye–eyewall interface as required;
    (c) measure the distance from storm center to this isotherm along the four cardinal directions (N, E, S, and W).
5) The IR-derived eye size is then given by the mean of the four distances.

The regression, which explains 60% of the RMW variance, is given by

$$RMW_{est} = a_0 + a_1 R_{eye},$$

where RMW_{est} is the estimated surface RMW (km), R_{eye} is the IR-measured eye size (km), and the coefficients are $a_0 = +2.8068$, $a_1 = +0.8361$.

In a dependent test on the sample data, the mean absolute error (MAE) of the estimated RMW was 4.7 km (sample size $N = 164$). The spatial resolution of the IR imagery is 4 km, so this is near the limit of reducing the mean error characteristics. However, as mentioned previously we expect the performance to be affected by transient but possibly large errors caused by eyewall replacement cycles and asymmetries. Another challenge to estimating RMW is the occurrence of "flat" tangential wind profiles, that is, cases where the wind decays very slowly with radius. In these cases, a small local wind increase at large radius can cause a large instantaneous jump in the RMW. This makes the operational utility of knowledge of the RMW somewhat questionable in such cases. Corbosiero et al. (2005) addressed this issue by defining a "radius of maximum slope change," which is typically the radius where the tangential wind first stops increasing with increasing radius and becomes flat or starts decreasing with radius. This is the radius that our algorithm tends to identify and in most cases it is collocated with the RMW.

As an independent test, the algorithm was executed in real time during the 2005 Atlantic hurricane season. Automated identification of clear eyes in the IR imagery was performed by the advanced Dvorak technique (ADT; Velden et al. 1998; Olander and Velden 2007), and in these cases, the RMW algorithm was executed every half-hour. Validation was performed against aircraft reconnaissance, which yielded 139 cases. The error distribution is shown in Fig. 1. As expected, we find that the algorithm is biased toward underestimating the RMW (bias = +6.7 km); the bias gives some indication of the systematic difference between the RMW and the radius of maximum slope change described above, which is expected to be less than or equal to the RMW in general. The MAE of the RMW estimates is 10.2 km. The mean relative error of the testing sample is 19% of the estimated RMW.

One application that has been found to benefit from the IR-estimated RMW is the Cooperative Institute for Meteorological Satellite Studies Advanced Microwave Sounding Unit (CIMSS-AMSU) algorithm (Brueske and Velden 2003), which is used operationally to estimate TC intensity. The algorithm relies on RMW information to serve as a proxy for eye size in order to mitigate subsampling issues due to the coarse resolu-

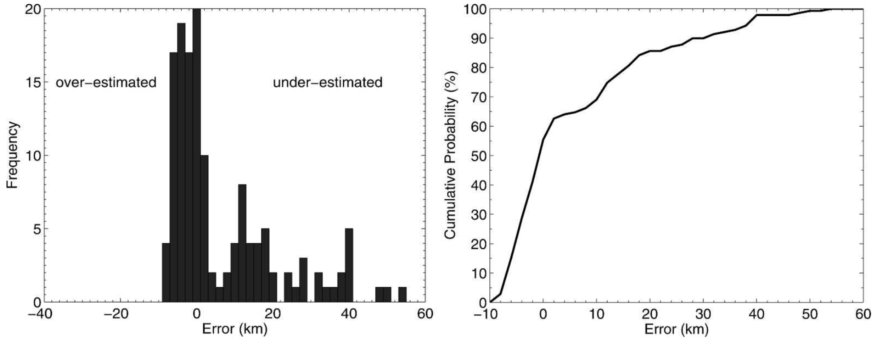

FIG. 1. Error distribution of RMW estimates in cases where a clear eye was identified (N = 139). The errors are based on independent real-time testing during the 2005 Atlantic hurricane season. Clear-eye cases were identified by the ADT.

tion of the instrument (Herndon and Velden 2004). This RMW information has been traditionally extracted from the Automated Tropical Cyclone Forecast (ATCF) system (Miller et al. 1990; Sampson and Schrader 2000). To measure the potential improvement in the CIMSS-AMSU algorithm, 55 cases from 2001 to 2004 were compared using RMW information from the ATCF system versus the IR-derived RMW from our algorithm. Using the RMW from the ATCF files, the MAE of the intensity estimates (measured as minimum sea level pressure) was 7.9 mb with a bias of +3.9 mb. Replacing the ATCF RMW with IR-measured RMW decreased the absolute error by 30% to 5.6 mb and the bias was reduced to −1.4 mb (errors are determined using contemporaneous aircraft reconnaissance minimum sea level pressure measurements). Because of the significant error reduction in the intensity estimates, starting in the 2005 season the CIMSS-AMSU intensity estimation algorithm began using the IR-estimated RMW, which are made available in real time by the ADT in clear-eye cases. More thorough testing is under way.

b. Direct estimation of R34, R50, R64, and RMW

Here we form a general algorithm for the direct calculation of the axisymmetric critical surface wind radii R34, R50, and R64 as well as RMW, but without the requirement of a clear eye in the IR imagery as considered in the previous section. For the construction of this algorithm, we applied extended best-track data and storm-centered IR imagery that has been averaged over 6-h periods to coincide with the synoptic periods of the extended best track. The extended best-track data were quality controlled (as discussed in Kimball and Mulekar 2004) to remove spurious cases that do not satisfy the required relations RMW $\leq$ R64, RMW $\leq$ R50, RMW $\leq$ R34, and R64 $<$ R50 $<$ R34. To establish a higher degree of confidence in the reported critical surface wind radii, we formed a subset of the extended best-track data in which all data points are within ±12 h of an aircraft reconnaissance fix.

The critical wind radii in the extended best track are identified in each storm quadrant (NE, SE, SW, and NW), which we averaged to form an estimate of the axisymmetric radii. The 6-hourly mean IR imagery was produced for the entire archive, which presently spans the period 1995–2004. This resulted in 2995 mean two-dimensional images, which were then reduced to 6-hourly mean radial profiles by azimuthally averaging the two-dimensional imagery around the storm center to a radius of 500 km. To extract the leading modes of the variability of the azimuthally averaged brightness temperature (BT) profiles, we performed principal component analysis (PCA) on the standardized sample. The leading modes and the variances they explain are shown in Fig. 2. The first mode (or empirical orthogonal function; EOF) has little spatial structure and is always the same sign. This mode represents the overall BT anomaly of the cloud shield. The expansion coefficient (or principal component; PC) associated with this mode would be negative (positive) for cases where the BT is colder (warmer) than average. It is found that the first PC is well correlated with $V_{\max}$ (with a negative correlation coefficient), which is in agreement with the basis of the Dvorak enhanced IR technique (Dvorak 1984); that is, colder cloud-top temperatures are associated with greater intensity. The remaining modes (EOFs 2 and 3) have more structure and change sign at various radii. For example, when PC3 is negative, the eye BT is warmer than average and the cloud-top BT in the region $110 \leq r \leq 360$ km is colder than average. Again in agreement with the basis of the Dvorak technique, we find that PC3 is well correlated with $V_{\max}$ (with a negative correlation coefficient); that is, warmer

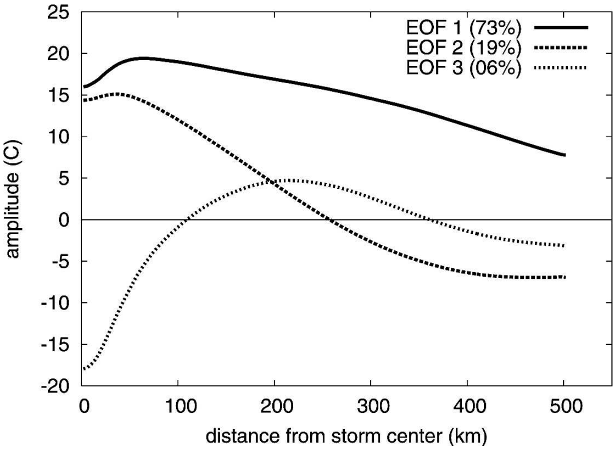

FIG. 2. Leading modes of variability (EOFs) of the 6-hourly mean azimuthally averaged profiles of IR BT. The variance explained by each EOF is shown in parentheses.

eyes and colder eyewall cloud tops are associated with greater intensity.

In addition to information about storm intensity, the EOFs contain information about the spatial structure of the convection occurring around the storms; each IR scene is represented by a particular linear combination of the EOFs, and the associated PCs contain concise information about eye size and the radial extent of the cirrus canopy and spiral bands. The relationship between convection and the local wind field is established (e.g., Samsury and Zipser 1995) and the EOFs are then expected to contain information about wind structure.

Our objective is to form estimates of critical wind radii with information from our datasets. Our a priori expectation, based on previous work (e.g., Shea and Gray 1973; Merrill 1984; Weatherford and Gray 1988a,b; Carr and Elsberry 1997; Cocks and Gray 2002; Croxford and Barnes 2002; Bell and Ray 2004; Kimball and Mulekar 2004), is that the critical wind radii will depend on $V_{\max}$, latitude ϕ (due to variations of the local Coriolis force), and storm age Δt measured as hours since reaching tropical storm intensity (due to the natural broadening of the wind field with time). For each critical wind radius, we first formed a multiple regression with the predictors $V_{\max}$, ϕ, and Δt, and to identify relationships between the critical wind radii and the IR imagery, we then added the IR-based PCs to the regression. Colinearity between the predictors of our regressions is not an issue: the PCs are orthogonal by construction and the largest correlation among the PCs and remaining predictors is 0.3.

Each regression was formed using a backward stepwise method. Backward stepwise regression begins with all the potential predictors in the model and removes the least significant predictors until all the remaining predictors are statistically significant. In our regressions, we require significance at the 99.9% or higher confidence level.

Table 1 shows the correlations with and without the inclusion of the IR-based PCs. The regressions are based on normalized predictors and predictands so that the relative contributions of each predictor can be demonstrated. Most of the variance of R34 is explained by $V_{\max}$, while ϕ and Δt explain lesser and roughly equal amounts. The relationship with Δt is a result of the "broadening" of the outer-core wind field with time, which often continues to occur well after maximum intensity (e.g., Cocks and Gray 2002). The regression without the PCs explains 44% of the variance of R34 and the MAE is 50.3 km. The mean relative error is 21% of the estimated R34. The MAE was calculated using a cumulative storm-by-storm jackknife procedure to better reflect the independently derived error: each storm was individually removed from the full sample and PCA was performed on the subsample of remaining storms. The regression was then trained on the subsample and tested on the storm that was left out. This was done for all storms in the sample and the cumulative errors were tallied. Since there is essentially no serial correlation between individual storms, this is a true independent test.

When the PCs are added, the regression explains 23% more total variance of R34 and the MAE decreases by 11%. The first two leading PCs contribute, but PC2 explains more variance. The third PC is not significant (none of the PCs of higher order than three were significant in any of the regressions in this section).

For the case of R50, Δt contributes roughly as much as $V_{\max}$ without the inclusion of the IR information. When the IR information is included, it is found that PC1 is not significant, but PC2 and PC3 contribute significantly, and PC2 explains more variance than any other predictor. With the inclusion of the IR, 32% more total variance is explained and MAE is reduced by 12%. In the case of R64, Δt plays a large role in the regression, as does PC2 when the IR information is included. The inclusion of the IR information reduces MAE by 9% and the variance explained increases from 32% to 43%.

The RMW does not depend on Δt and the sign of the correlation with $V_{\max}$ switches from positive to negative, in agreement with previous studies that generally show a contraction of the maximum wind concurrent with intensification. When the IR information is included, $V_{\max}$ and PC2 contribute the greatest share, the total variance explained increases from 20% to 34% (70% change), and MAE is reduced by 8% to 20.1 km.

TABLE 1. Description of critical wind radii regressions. Column one identifies the wind radius and the number of points in the sample (N). Columns 2–7 show normalized regression coefficients. Columns 2–4 show the contributions from $V_{\max}$, latitude (ϕ), and storm age (Δt), and columns 5–7 show contributions from the IR imagery. Regressions without and with the IR-based predictors, respectively, are shown in the first and second rows for each wind radius. Columns 8–9 show the R^2 statistic and MAE. The MAE was calculated independently in a storm-by-storm jackknife procedure. The percentage change due to the addition of the IR-based predictors are shown in parentheses. All predictors are significant at the 99.9% confidence level or greater ("n/s" indicates that a predictor was not significant).

	$V_{\max}$	ϕ	Δt	PC1	PC2	PC3	R^2	MAE (km)
R34	+0.45	+0.22	+0.26				0.44	50.3
$N = 1192$	+0.41	+0.23	+0.23	−0.16	+0.27	n/s	0.54 (23%)	44.8 (11%)
R50	+0.33	+0.20	+0.34				0.37	41.4
$N = 891$	+0.30	+0.20	+0.25	n/s	+0.34	−0.14	0.49 (32%)	36.6 (12%)
R64	+0.22	+0.20	+0.39				0.32	29.7
$N = 671$	+0.12	+0.16	+0.30	n/s	+0.34	−0.16	0.43 (34%)	26.9 (9%)
RMW	−0.38	+0.20	n/s				0.20	23.0
$N = 1251$	−0.41	+0.13	n/s	n/s	+0.33	−0.19	0.34 (70%)	21.1 (8%)

This can be compared to the MAE of 10.2 km calculated for the clear-eye cases in section 2a.

The distribution of error for the estimation of each wind radius when all significant predictors are included is shown in Fig. 3. The errors are based on our cumulative storm-by-storm jackknife procedure. It should be noted that there are no physical constraints on these estimates and thus it is mathematically possible that independent combinations of the estimated wind radii may be unphysical in practice. For example, there could be cases where R34 < R50, or less obviously, there may be cases where a combination of estimated radii would yield a wind profile that is locally inertially unstable (caused by an overly rapid decay with increasing radius). Quality checking is recommended and could be quickly performed operationally. Of course, R50 and R64 should not be estimated for cases when $V_{\max} < 50$ or 64 kt, respectively.

Table 2 gives the dimensional regression coefficients that can be used in real time or postanalysis to estimate R34, R50, R64, and RMW (all in units of kilometers), where $V_{\max}$ has units of knots, ϕ has units of degrees, and Δt is the number of hours since reaching tropical storm intensity. The PCs are calculated by projecting the standardized BT profiles onto the EOFs. All the data necessary to perform this calculation can be easily contained in a small data file.

c. *Estimation of inner-core two-dimensional surface wind fields*

Here, we construct an algorithm that estimates tangential wind profiles in the disk $2 \leq r \leq 182$ km and then adds a motion-based asymmetry to create a complete two-dimensional wind field. The datasets used are described in detail in Mueller et al. (2006) and consist of 12-h mean IR imagery and flight-level wind profiles combined with working best-track information regarding intensity $V_{\max}$ and latitude ϕ. The data spans 456 cases from 94 storms during the period 1995–2004. Similar to the previous section, the 12-h mean IR imagery was azimuthally averaged about the translating storm center and then decomposed into EOFs. The 12-h azimuthal mean flight-level wind profiles span the disk $2 \leq r \leq 182$ in 4-km increments. The span of the profiles was constrained to lie within 182 km by the standard flight patterns of the aircraft. For each radius, we regressed the flight-level tangential wind at that radius onto $V_{\max}$, ϕ, and the first five leading PCs from the IR profiles. The regression of the wind profiles onto the PCs is referred to as single-field principle component analysis (SFPCA; Bretherton et al. 1992) and is well suited for reconstructing the variance of the predictand field. The leading five PCs were chosen based on a minimization of the cumulative error in a storm-by-storm jackknife procedure using all 94 storms in the dataset. Our method for constructing estimated wind profiles produces relatively unconstrained profile shapes and, thus, represents a significantly different approach compared to previous studies that require fitting the profiles to various parametric models (Holland 1980; Willoughby and Rahn 2004; Mueller et al. 2006).

To identify the relative contributions of the predictors in the regression, we normalized the coefficients of the regression at each radius (Fig. 4). The predictor $V_{\max}$ dominates the regression at all radii and is fairly constant beyond $r \sim 20$ km. Latitude is the next most important contributor at all radii beyond 50 km and increases in importance with increasing distance from the storm center. The PCs combine to contribute significantly at all radii, but PC2 and PC3 tend to explain

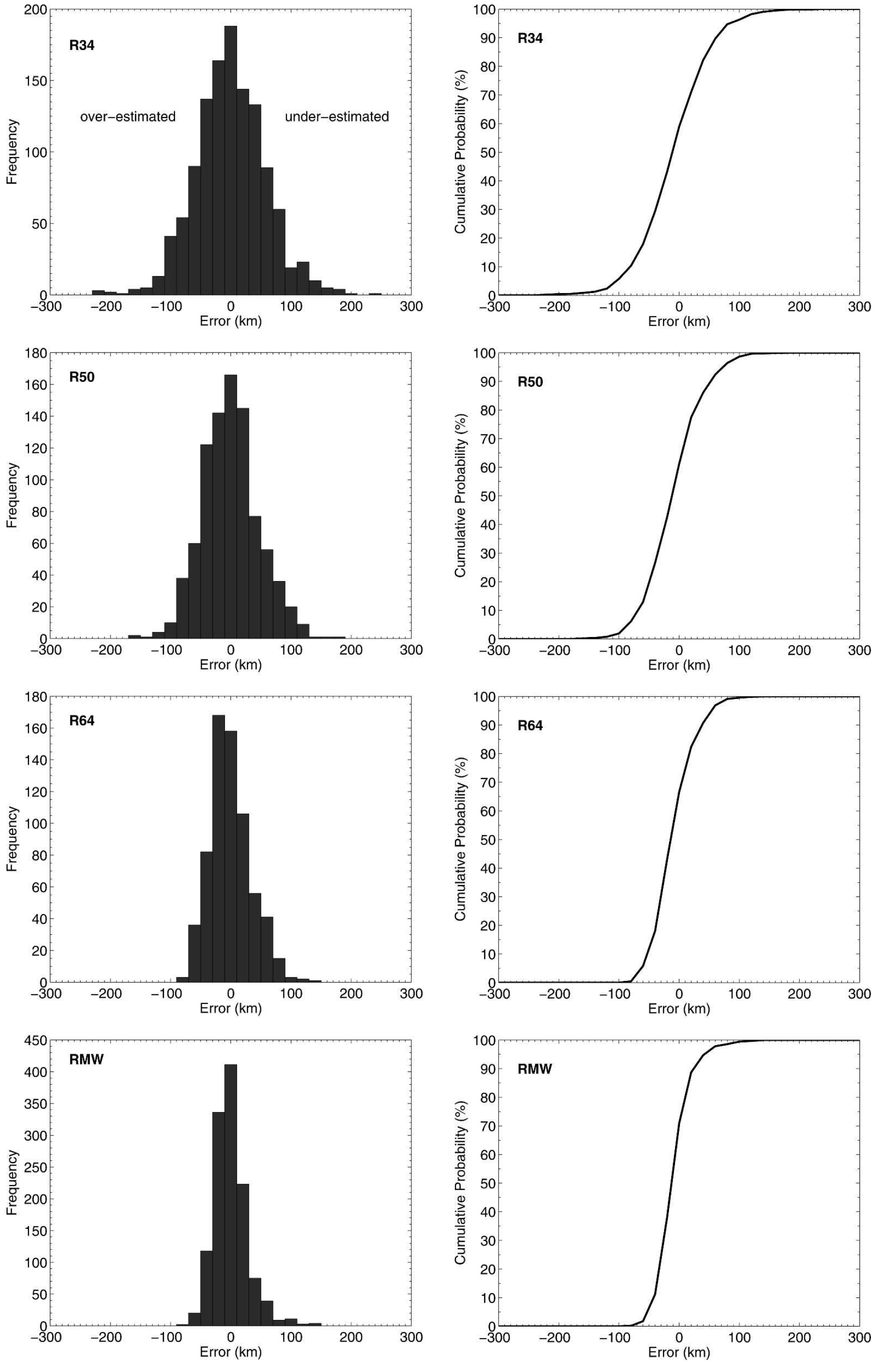

FIG. 3. Error distributions, based on cumulative storm-by-storm jackknife testing, for the estimates of R34, R50, R64, and RMW.

the most variance. At the outer radii, PC2 is the dominant IR-based predictor.

We performed two independent tests on the algorithm. For the first test, we trained the regressions using 455 cases from 87 storms during 1995–2003 and then tested the method on 51 cases from 7 storms in 2004. The overall results are shown in Fig. 5 and demonstrate that the method does a reasonable job of capturing the basic shape of the wind profiles. Figure 6 shows the MAE at each radius along the estimated profile. Similar to the previous section, we performed our analyses with and without the inclusion of the PCs in order to measure how much additional skill the IR imagery introduces to the estimates. As expected, the largest er-

TABLE 2. Dimensional coefficients for the critical wind radii regressions. See Table 1 for symbol definitions.

	y intercept	$V_{\max}$	ϕ	Δt	PC1	PC2	PC3
R34	+19.6305	+1.1830	+2.9320	+0.2380	−1.3930	+4.6974	n/s
R50	+5.1766	+0.7409	+1.9060	+0.2073	n/s	+4.7188	−3.0062
R64	+20.0819	+0.2345	+1.0907	+0.1865	n/s	+3.3293	−2.3511
RMW	+75.5154	−0.4813	+0.6992	n/s	n/s	+2.4101	−2.4358

rors are found at radii where the strongest maximum winds and strongest gradients tend to occur but this is also the region where the IR information helps the most. At these radii, the relationship between the wind, $V_{\max}$, and latitude, which reflects a kind of climatology, is most strongly nudged by the information in the PCs. This is particularly true in cases when an eye is evident in the IR imagery, which would be reflected in the values of PC2 and higher. At larger radii, the error profile is flatter and the IR reduces error fairly uniformly out to the end of the data ($r = 182$ km). The local minimum near $r = 40$ km is apparently not meaningful and does not remain evident in the jackknife test described below. The mean MAE for the profile is 9.6 kt (4.9 m s^{-1}) without the PCs and 8.4 kt (4.3 m s^{-1}) when the IR information is included (a 13% overall error reduction). For comparison with the results of Mueller et al. (2006), the error in the estimated RMW versus the aircraft-measured RMW was 21.9 km without the IR and 18.8 km with the IR included.

As a more thorough test of the algorithm, we performed a cumulative storm-by-storm jackknife procedure. The error, shown in Fig. 7, is lower at all radii when compared to Fig. 6, but the reduction of error by the inclusion of the IR information is less overall, and ranges from 10% near $r = 20$ km to 3% at $r = 182$ km. The mean MAE for the profile is 7.6 kt and the mean error reduction for the profile by the inclusion of the IR information is 3.8%. If we repeat these analyses for weaker hurricanes (Saffir–Simpson categories 1 and 2), the profile-mean MAE is 7.6 kt and the mean error reduction is 2.4%. For major hurricanes (Saffir–Simpson category 3 or stronger), the profile-mean MAE is 10.0 kt and the mean error reduction by the inclusion of the PCs increases significantly to 17.5%. Thus, the inclusion of the IR information has a much greater positive effect in stronger storms.

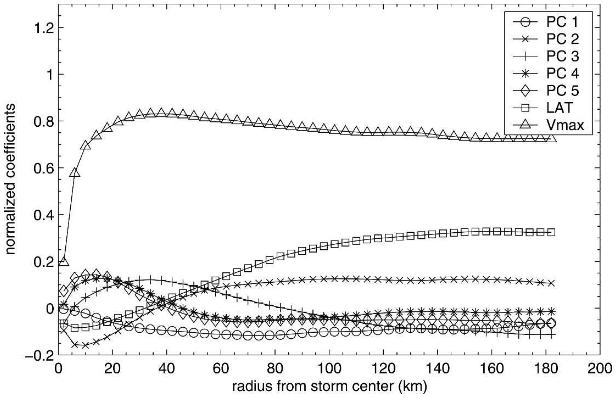

FIG. 4. Normalized coefficients for the SFPCA-regression algorithm at each radius.

The next steps in constructing an algorithm to estimate the full two-dimensional surface wind field are the reduction of the estimated flight-level wind profiles to profiles of 10-m sustained winds and the addition of a storm-motion-based wavenumber-one asymmetry. The reduction to the surface was performed using a constant reduction factor of 0.9 and the motion vector was calculated from the working best-track position fixes. The constant reduction factor was used due to the absence of vertical wind information in our datasets (cf. Franklin et al. 2003).

An example of the final product applied to Hurricane Jeanne (2004) is shown in Fig. 8. At this time (0600 UTC 25 September), Jeanne was moving westward at 12 kt toward the Florida coast as a category 2 storm with $V_{\max}$ increasing from 85 to 90 kt during the previous 6-h period. The critical wind radii R34, R50, and R64 in the figure are identified by the dashed contours. Because the analyses are constrained to a disk of radius 182 km, there will often be times when critical wind radii lie outside the analyses. For example, in Fig. 8 most of R34 and a significant portion of R50 are beyond the analysis region. To improve the utility of the algorithm, and as a first informal step toward a complete error analysis of the two-dimensional fields, our next step was to introduce our inner-core winds into the existing NOAA/HRD H*Wind system (Powell and Houston 1996; Powell et al. 1996; Powell et al. 1998; Dunion et al. 2003), which traditionally relies on the availability of flight-level aircraft data in the inner core. This allowed us to blend our winds with additional data from the outer core [SSM/I, Quick Scatterometer (QuikScat), Geostationary Operational Environmental Satellite (GOES) cloud-feature track, and buoy reports] to create a much broader and complete analysis

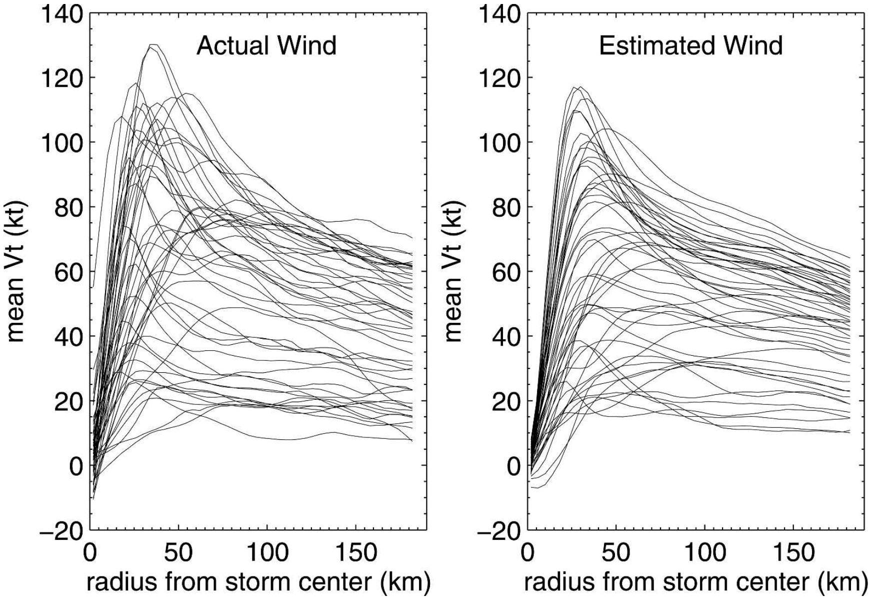

FIG. 5. (left) Aircraft-measured tangential wind profiles vs (right) estimated wind profiles. The profiles represent 12-h mean azimuthal averages. The estimated wind profiles are based on independent testing on 51 cases from seven storms during the 2004 hurricane season.

and make comparisons between wind fields derived from aircraft flight-level data and wind fields estimated by our algorithm.

An example is shown in Fig. 9 for the case in Hurricane Jeanne (2004) discussed above and shown in Fig. 8. The panels on the left show the wind fields deduced with the IR-based wind estimates in the inner-core in place of the aircraft data. The right panels are based on the use of flight-level data in the inner core. When the aircraft data are replaced with our estimated IR-based winds, the overall wind field is comparable, in magnitude and shape, to the analysis with the aircraft data. The largest errors are found to the south of the storm center and the smallest errors are found to the west. The position of the maximum wind is very well estimated [indicated by the plus (+) sign 32 km northwest of center], but the magnitude is too weak (80 versus 87 kt with the aircraft data). The IR-based winds tend to

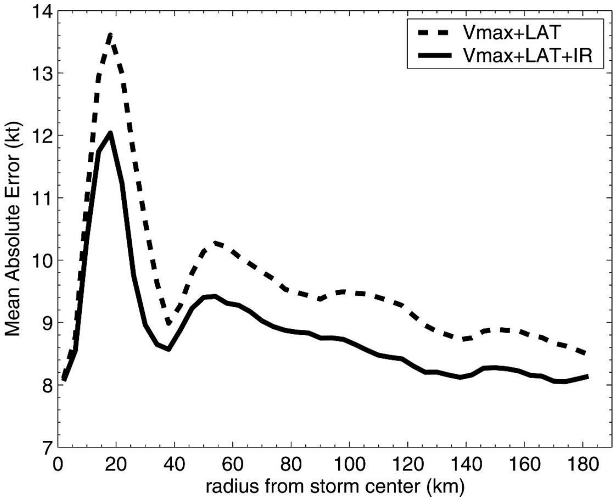

FIG. 6. Profiles of MAE (kt) for the estimated wind profiles in the 2004 independent test. The solid (dashed) curve shows error with (without) the inclusion of the IR information.

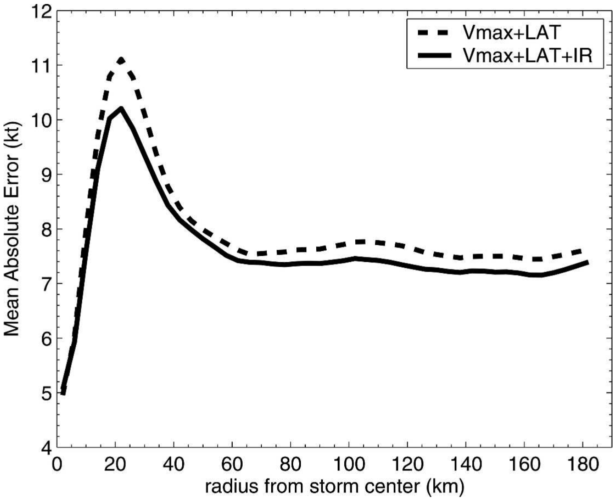

FIG. 7. Same as in Fig. 6 but for the jackknife test.

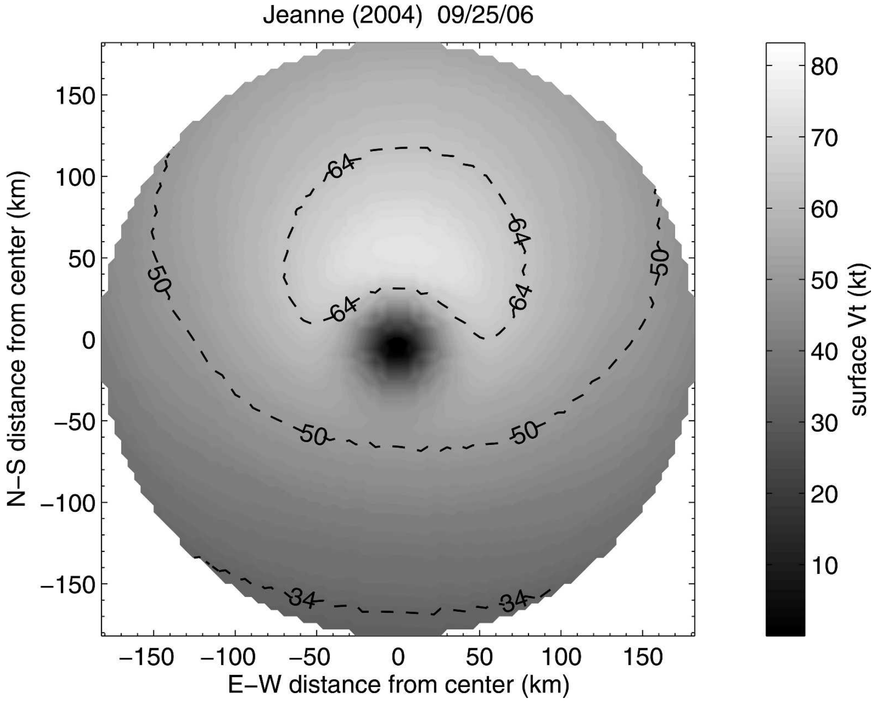

FIG. 8. Two-dimensional tangential wind field estimate in Hurricane Jeanne at 0600 UTC 25 Sep 2004. The critical wind radii R34, R50, and R64 are shown by the dashed contours.

be too weak almost everywhere, which causes the critical wind radii to be generally too small. More thorough testing is warranted, and this algorithm will be more quantitatively tested during the 2006 season.

The two-dimensional wind estimates described here will also be utilized in a recently developed NOAA demonstration project to provide multiplatform satellite-based wind estimates globally in and around TCs. The wind analyses are created by a fully automated variational system that makes use of SSM/I, QuikScat, cloud-feature tracked (Velden et al. 2005), AMSU-based (Bessho et al. 2006), and IR-based (Mueller et al. 2006) wind estimates (Knaff and DeMaria 2006).

3. Summary

We have introduced three new algorithms that utilize IR satellite information to estimate various metrics of tropical cyclone surface wind fields with an emphasis on the inner core—an area that traditionally relies on aircraft reconnaissance for wind measurements.

For cases when a clear symmetric eye is present in the IR imagery, we quantified a simple relationship between IR-measured eye size and RMW, and found that our estimates of RMW helped reduce intensity estimate error in an existing AMSU-based algorithm.

For the general case with no IR scene constraints, we formed regressions that provide estimates of critical wind radii R34, R50, R64, and RMW. We demonstrated that IR imagery does contain significant information about the underlying wind fields, in spite of the opacity (at IR wavelengths) of the cirrus canopy that typically resides over storms. The IR information was extracted by reducing two-dimensional brightness temperature fields to azimuthally averaged profiles and then further reducing the profiles through principle component analysis. This allowed us to use the principle components as predictors in the regressions.

To estimate complete two-dimensional surface wind fields, we applied single-field principle component analysis to contemporaneous profiles of IR brightness temperature and flight-level wind profiles. This produced wind profile estimates to which we added a simple motion-based wind asymmetry. These wind fields can serve to fill the data-void inner-core region when aircraft reconnaissance is not available, and can be added to existing wind algorithms that blend inner-core and outer-core data into fully encompassing wind fields.

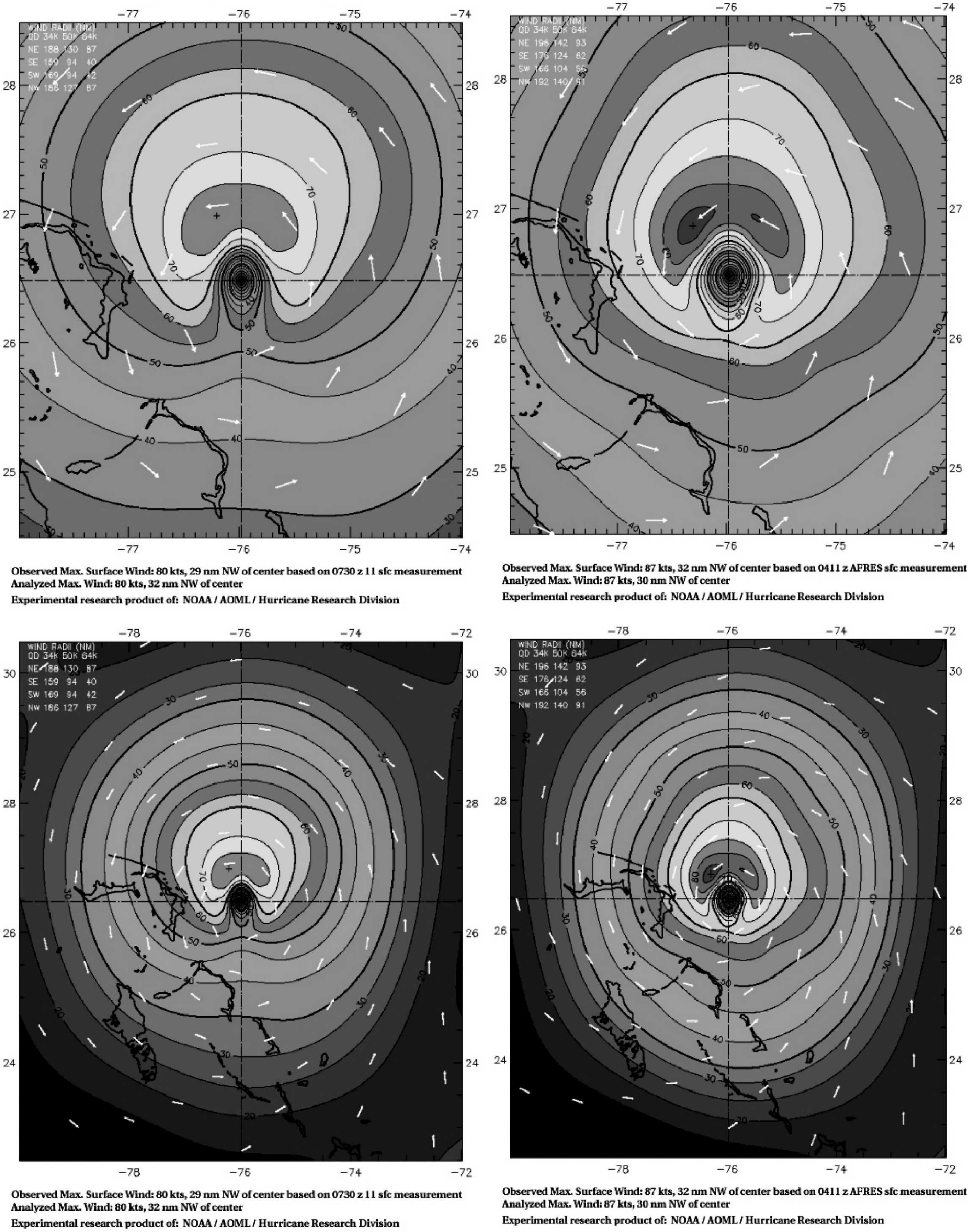

Observed Max. Surface Wind: 80 kts, 29 nm NW of center based on 0730 z 11 sfc measurement
Analyzed Max. Wind: 80 kts, 32 nm NW of center
Experimental research product of: NOAA / AOML / Hurricane Research Division

Observed Max. Surface Wind: 87 kts, 32 nm NW of center based on 0411 z AFRES sfc measurement
Analyzed Max. Wind: 87 kts, 30 nm NW of center
Experimental research product of: NOAA / AOML / Hurricane Research Division

Observed Max. Surface Wind: 80 kts, 29 nm NW of center based on 0730 z 11 sfc measurement
Analyzed Max. Wind: 80 kts, 32 nm NW of center
Experimental research product of: NOAA / AOML / Hurricane Research Division

Observed Max. Surface Wind: 87 kts, 32 nm NW of center based on 0411 z AFRES sfc measurement
Analyzed Max. Wind: 87 kts, 30 nm NW of center
Experimental research product of: NOAA / AOML / Hurricane Research Division

FIG. 9. NOAA/HRD H*Wind maximum 1-min sustained surface wind analyses (kt) for the case of Hurricane Jeanne shown in Fig. 8. (left) The analyses using the IR-based wind field in place of the aircraft flight-level data in the inner core. (right) The analyses with the flight-level data in the inner core. (top) The 4° analyses and (bottom) the 8° analyses, showing the spatial extent of the analyses.

Acknowledgments. We thank Sonia Otero, Jason Dunion, and Mark Powell for their assistance with the NOAA/HRD H*Wind system, and Mark DeMaria and Russ Elsberry for their valuable input. We are also grateful to Tim Olander for his assistance with the advanced Dvorak technique. This work has been supported by NRL-MRY Satellite Applications Grant N00173-01-C-2024, and Grant RPI03-3-001 from the Risk Prediction Initiative, Bermuda Biological Station for Research, Inc.

REFERENCES

Aberson, S. D., 2002: Two years of operational hurricane synoptic surveillance. *Wea. Forecasting,* **17,** 1101–1110.

——, and J. L. Franklin, 1999: Impact on hurricane track and intensity forecasts of GPS dropwindsonde observations from the first-season flights of the NOAA Gulfstream-IV jet aircraft. *Bull. Amer. Meteor. Soc.,* **80,** 421–427.

Bell, K., and P. S. Ray, 2004: North Atlantic hurricanes 1977–99: Surface hurricane-force wind radii. *Mon. Wea. Rev.,* **132,** 1167–1189.

Bessho, K., M. DeMaria, and J. A. Knaff, 2006: Tropical cyclone wind retrievals from the Advanced Microwave Sounder Unit (AMSU): Application to surface wind analysis. *J. Appl. Meteor. Climatol.,* **45,** 399–415.

Bretherton, C. S., C. Smith, and J. M. Wallace, 1992: An intercomparison of methods for finding coupled patterns in climate data. *J. Climate,* **5,** 541–560.

Brueske, K. F., and C. S. Velden, 2003: Satellite-based tropical cyclone intensity estimation using the NOAA-KLM series Advanced Microwave Sounding Unit (AMSU). *Mon. Wea. Rev.,* **131,** 687–697.

Carr, L. E., III, and R. L. Elsberry, 1997: Models of tropical cyclone wind distribution and beta-effect propagation for application to tropical cyclone track forecasting. *Mon. Wea. Rev.,* **125,** 3190–3209.

Cocks, S. B., and W. M. Gray, 2002: Variability of the outer wind profiles of western North Pacific typhoons: Classifications and techniques for analysis and forecasting. *Mon. Wea. Rev.,* **130,** 1989–2005.

Corbosiero, K. L., J. Molinari, and M. L. Black, 2005: The structure and evolution of Hurricane Elena (1985). Part I: Symmetric intensification. *Mon. Wea. Rev.,* **133,** 2905–2921.

Croxford, M., and G. M. Barnes, 2002: Inner core strength of Atlantic tropical cyclones. *Mon. Wea. Rev.,* **130,** 127–139.

Dunion, J. P., and C. S. Velden, 2002: Application of surface-adjusted GOES low-level cloud-drift winds in the environment of Atlantic tropical cyclones. Part I: Methodology and validation. *Mon. Wea. Rev.,* **130,** 1333–1346.

——, S. H. Houston, C. S. Velden, and M. D. Powell, 2002: Application of surface-adjusted GOES low-level cloud-drift winds in the environment of Atlantic tropical cyclones. Part II: Integration into surface wind analyses. *Mon. Wea. Rev.,* **130,** 1347–1355.

——, C. W. Landsea, S. H. Houston, and M. D. Powell, 2003: A reanalysis of the surface winds for Hurricane Donna of 1960. *Mon. Wea. Rev.,* **131,** 1992–2011.

Dvorak, V. F., 1984: Tropical cyclone intensity analysis using satellite data. NOAA Tech. Rep. NESDIS 11, 47 pp. [Available from NOAA/NESDIS, 5200 Auth Rd., Washington, DC 20233.]

Franklin, J. L., M. L. Black, and K. Valde, 2003: GPS dropwindsonde wind profiles in hurricanes and their operational implications. *Wea. Forecasting,* **18,** 32–44.

Goodberlet, M. A., C. T. Swift, and J. C. Wilkerson, 1989: Remote sensing of ocean surface winds with the Special Sensor Microwave/Imager. *J. Geophys. Res.,* **94,** 14 547–14 555.

Herndon, D. H., and C. S. Velden, 2004: Upgrades to the UW-CIMSS AMSU-based tropical cyclone intensity algorithm. Preprints, *26th Conf. on Hurricanes and Tropical Meteorology,* Miami, FL, Amer. Meteor. Soc., CD-ROM, 4D.1.

Hock, T. F., and J. L. Franklin, 1999: The NCAR GPS dropwindsonde. *Bull. Amer. Meteor. Soc.,* **80,** 407–420.

Holland, G. J., 1980: An analytic model of the wind and pressure profiles in hurricanes. *Mon. Wea. Rev.,* **108,** 1212–1218.

Jarvinen, B. R., C. J. Neumann, and M. A. S. Davis, 1984: A tropical cyclone data tape for the North Atlantic Basin, 1886–1983: Contents, limitations and uses. NOAA Tech. Memo. NWS NHC 22, NOAA/National Hurricane Center, Miami, FL, 21 pp. [Available from NOAA/Tropical Prediction Center, 11691 SW 17th St., Miami, FL 33165–2149.]

Jorgensen, D. P., 1984: Mesoscale and convective-scale characteristics of mature hurricanes. Part I: General observations by research aircraft. *J. Atmos. Sci.,* **41,** 1268–1285.

——, E. J. Zipser, and M. A. LeMone, 1985: Vertical motion in intense hurricanes. *J. Atmos. Sci.,* **42,** 839–856.

Kimball, S. K., and M. S. Mulekar, 2004: A 15-year climatology of North Atlantic tropical cyclones. Part I: Size parameters. *J. Climate,* **17,** 3555–3575.

Knaff, J. A., and M. DeMaria, 2006: A multi-platform satellite tropical cyclone wind analysis system. Preprints, *14th Conf. on Satellite Meteorology and Oceanography,* Atlanta, GA, Amer. Meteor. Soc., CD-ROM, P4.9.

Kossin, J. P., 2002: Daily hurricane variability inferred from GOES infrared imagery. *Mon. Wea. Rev.,* **130,** 2260–2270.

——, and M. D. Eastin, 2001: Two distinct regimes in the kinematic and thermodynamic structure of the hurricane eye and eyewall. *J. Atmos. Sci.,* **58,** 1079–1090.

——, W. H. Schubert, and M. T. Montgomery, 2000: Unstable interactions between a hurricane's primary eyewall and a secondary ring of enhanced vorticity. *J. Atmos. Sci.,* **57,** 3893–3917.

Marks, F. D., Jr., 2003: State of the science: Radar view of tropical cyclones. *Radar and Atmospheric Science: A Collection of Essays in Honor of David Atlas, Meteor. Monogr.,* No. 52, Amer. Meteor. Soc., 33–74.

Merrill, R. T., 1984: A Comparison of large and small tropical cyclones. *Mon. Wea. Rev.,* **112,** 1408–1418.

Miller, R. J., A. J. Schrader, C. R. Sampson, and T. L. Tsui, 1990: The Automated Tropical Cyclone Forecasting System (ATCF). *Wea. Forecasting,* **5,** 653–660.

Mueller, K. J., M. DeMaria, J. A. Knaff, J. P. Kossin, and T. H. Vonder Haar, 2006: Objective estimation of tropical cyclone wind structure from infrared satellite data. *Wea. Forecasting,* **21,** 907–922.

Olander, T. L., and C. S. Velden, 2007: The advanced Dvorak technique: Continued development of an objective scheme to estimate tropical cyclone intensity using geostationary infrared satellite imagery. *Wea. Forecasting,* in press.

Powell, M. D., and S. H. Houston, 1996: Hurricane Andrew's landfall in south Florida. Part II: Surface wind fields and potential real-time applications. *Wea. Forecasting,* **11,** 329–349.

——, ——, and T. A. Reinhold, 1996: Hurricane Andrew's landfall in south Florida. Part I: Standardizing measurements for documentation of surface wind fields. *Wea. Forecasting,* **11,** 304–328.

——, ——, L. R. Amat, and N. Morisseau-Leroy, 1998: The HRD real-time hurricane wind analysis system. *J. Wind Eng. Indust. Aerodyn.,* **77–78,** 53–64.

Reasor, P. D., M. T. Montgomery, F. D. Marks Jr., and J. F. Gamache, 2000: Low-wavenumber structure and evolution of the hurricane inner core observed by airborne dual-Doppler radar. *Mon. Wea. Rev.,* **128,** 1653–1680.

Rozoff, C. M., W. H. Schubert, B. D. McNoldy, and J. P. Kossin, 2006: Rapid filamentation zones in intense tropical cyclones. *J. Atmos. Sci.,* **63,** 325–340.

Sampson, C. R., and A. J. Schrader, 2000: The Automated Tropical Cyclone Forecasting System (version 3.2). *Bull. Amer. Meteor. Soc.,* **81,** 1231–1240.

Samsury, C. E., and E. J. Zipser, 1995: Secondary wind maxima in hurricanes: Airflow and relationship to rainbands. *Mon. Wea. Rev.,* **123,** 3502–3517.

Shapiro, L. J., and H. E. Willoughby, 1982: The response of balanced hurricanes to local sources of heat and momentum. *J. Atmos. Sci.,* **39,** 378–394.

Shea, D. J., and W. M. Gray, 1973: The hurricane's inner core region. I. Symmetric and asymmetric structure. *J. Atmos. Sci.,* **30,** 1544–1564.

Uhlhorn, E. W., and P. G. Black, 2003: Verification of remotely sensed sea surface winds in hurricanes. *J. Atmos. Oceanic Technol.,* **20,** 99–116.

Velden, C. S., T. L. Olander, and R. M. Zehr, 1998: Development of an objective scheme to estimate tropical cyclone intensity from digital geostationary satellite infrared imagery. *Wea. Forecasting,* **13,** 172–186.

——, and Coauthors, 2005: Recent innovations in deriving tropospheric winds from meteorological satellites. *Bull. Amer. Meteor. Soc.,* **86,** 205–223.

Weatherford, C. L., and W. M. Gray, 1988a: Typhoon structure as revealed by aircraft reconnaissance. Part I: Data analysis and climatology. *Mon. Wea. Rev.,* **116,** 1032–1043.

——, and ——, 1988b: Typhoon structure as revealed by aircraft reconnaissance. Part II: Structural variability. *Mon. Wea. Rev.,* **116,** 1044–1056.

Weissman, D. E., M. A. Bourassa, and J. Tongue, 2002: Effects of rain rate and wind magnitude on SeaWinds scatterometer wind speed errors. *J. Atmos. Oceanic Technol.,* **19,** 738–746.

Willoughby, H. E., 1998: Tropical cyclone eye thermodynamics. *Mon. Wea. Rev.,* **126,** 3053–3067.

——, and M. E. Rahn, 2004: Parametric representation of the primary hurricane vortex. Part I: Observations and evaluation of the Holland (1980) model. *Mon. Wea. Rev.,* **132,** 3033–3048.

——, J. A. Clos, and M. G. Shoreibah, 1982: Concentric eyewalls, secondary wind maxima, and the evolution of the hurricane vortex. *J. Atmos. Sci.,* **39,** 395–411.

Wu, C.-C., and Coauthors, 2005: Dropwindsonde Observations for Typhoon Surveillance near the Taiwan Region (DOTSTAR): An overview. *Bull. Amer. Meteor. Soc.,* **86,** 787–790.

Yueh, S. H., B. W. Stiles, and W. T. Liu, 2003: QuikSCAT wind retrievals for tropical cyclones. *IEEE Trans. Geosci. Remote Sens.,* **41,** 2616–2628.

Zehr, R. M., 2000: Tropical cyclone research using large infrared image data sets. Preprints, *24th Conf. on Hurricanes and Tropical Meteorology,* Fort Lauderdale, FL, Amer. Meteor. Soc., 486–487.

Zeng, L., and R. A. Brown, 1998: Scatterometer observations at high wind speeds. *J. Appl. Meteor.,* **37,** 1412–1420.